Research Article | Vol. 8, No. 11 | 1 Nov 2017 | BIOMEDICAL OPTICS EXPRESS 5127
Biomedical Optics EXPRESS

Ultrahigh-resolution optical coherence elastography through a micro-endoscope: towards *in vivo* imaging of cellular-scale mechanics

QI FANG,[1,2,*] ANDREA CURATOLO,[1,2] PHILIP WIJESINGHE,[1,3] YEN LING YEOW,[4] JULIANA HAMZAH,[4] PETER B. NOBLE,[5,6] KAROL KARNOWSKI,[3] DAVID D. SAMPSON,[3,7] RUTH GANSS,[8] JUN KI KIM,[9] WOEI M. LEE,[10,11] AND BRENDAN F. KENNEDY[1,2]

[1]*BRITElab, Harry Perkins Institute of Medical Research, QEII Medical Centre, Nedlands and Centre for Medical Research, The University of Western Australia, Perth, Western Australia 6009, Australia*
[2]*School of Electrical, Electronic & Computer Engineering, The University of Western Australia, Perth, Western Australia 6009, Australia*
[3]*Optical+Biomedical Engineering Laboratory, School of Electrical, Electronic & Computer Engineering, The University of Western Australia, Perth, Western Australia 6009, Australia*
[4]*Targeted Drug Delivery, Imaging and Therapy, Harry Perkins Institute of Medical Research, QEII Medical Centre, Nedlands and Centre for Medical Research, The University of Western Australia, Perth, Western Australia 6009, Australia*
[5]*School of Human Sciences, The University of Western Australia, Perth, Western Australia 6009, Australia*
[6]*Centre for Neonatal Research & Education, School of Paediatrics and Child Health, The University of Western Australia, Perth, Western Australia 6009, Australia*
[7]*Centre for Microscopy, Characterisation & Analysis, The University of Western Australia, Perth, Western Australia 6009, Australia*
[8]*Vascular Biology and Stromal Targeting, Harry Perkins Institute of Medical Research, QEII Medical Centre, Nedlands and Centre for Medical Research, The University of Western Australia, Perth, Western Australia 6009, Australia*
[9]*Biomedical Engineering Research Center, Asan Institute for Life Sciences, Asan Medical Center, and University of Ulsan College of Medicine, Seoul, 138-736, South Korea*
[10]*Research School of Engineering, College of Engineering and Computer Science, The Australian National University, Canberra ACT 0200, Australia*
[11]*The ARC Centre of Excellence in Advanced Molecular Imaging, The Australian National University, ACT 2601, Australia*
[*]*qi.fang@uwa.edu.au*

Abstract: In this paper, we describe a technique capable of visualizing mechanical properties at the cellular scale deep in living tissue, by incorporating a gradient-index (GRIN)-lens micro-endoscope into an ultrahigh-resolution optical coherence elastography system. The optical system, after the endoscope, has a lateral resolution of 1.6 μm and an axial resolution of 2.2 μm. Bessel beam illumination and Gaussian mode detection are used to provide an extended depth-of-field of 80 μm, which is a 4-fold improvement over a fully Gaussian beam case with the same lateral resolution. Using this system, we demonstrate quantitative elasticity imaging of a soft silicone phantom containing a stiff inclusion and a freshly excised malignant murine pancreatic tumor. We also demonstrate qualitative strain imaging below the tissue surface on *in situ* murine muscle. The approach we introduce here can provide high-quality extended-focus images through a micro-endoscope with potential to measure cellular-scale mechanics deep in tissue. We believe this tool is promising for studying biological processes and disease progression *in vivo*.

OCIS codes: (110.4500) Optical coherence tomography; (170.2150) Endoscopic imaging; (170.3880) Medical and biological imaging.

#304351 https://doi.org/10.1364/BOE.8.005127
Journal © 2017 Received 9 Aug 2017; revised 24 Sep 2017; accepted 1 Oct 2017; published 20 Oct 2017
Corrected: 24 October 2017

Biomedical Optics EXPRESS

References and links

1. P. A. Janmey and C. A. McCulloch, "Cell mechanics: integrating cell responses to mechanical stimuli," Annu. Rev. Biomed. Eng. **9**, 1–34 (2007).
2. J. F. Greenleaf, M. Fatemi, and M. Insana, "Selected methods for imaging elastic properties of biological tissues," Annu. Rev. Biomed. Eng. **5**, 57–78 (2003).
3. A. P. Sarvazyan, O. V. Rudenko, S. D. Swanson, J. B. Fowlkes, and S. Y. Emelianov, "Shear wave elasticity imaging: a new ultrasonic technology of medical diagnostics," Ultrasound Med. Biol. **24**(9), 1419–1435 (1998).
4. R. Muthupillai and R. L. Ehman, "Magnetic resonance elastography," Nat. Med. **2**, 601–603 (1996).
5. H.-J. Butt, B. Cappella, and M. Kappl, "Force measurements with the atomic force microscope: Technique, interpretation and applications," Surf. Sci. Rep. **59**(1-6), 1–152 (2005).
6. S. Munevar, Y. Wang, and M. Dembo. "Traction force microscopy of migrating normal and H-ras transformed 3T3 fibroblasts," Biophys. J., **80**(4), 1744–1757 (2001).
7. J. M. Schmitt, "OCT elastography: imaging microscopic deformation and strain of tissue," Opt. Express **3**(6), 199–211 (1998).
8. G. Scarcelli and S. H. Yun, "Confocal Brillouin microscopy for three-dimensional mechanical imaging," Nat. Photon. **2**, 39–43 (2008).
9. Z. Hajjarian and S. K. Nadkarni, "Evaluating the viscoelastic properties of tissue from laser speckle fluctuations," Sci. Rep. **2**, 316 (2012).
10. B. F. Kennedy, K. M. Kennedy, and D. D. Sampson, "A review of optical coherence elastography: fundamentals, techniques and prospects," IEEE J. Sel. Top. Quantun Electron. **20**(2), 7101217 (2014).
11. K. Larin and D. D. Sampson, "Optical coherence elastography - OCT at work in tissue biomechanics," Biomed. Opt. Express **8**(2), 1172–1202 (2017).
12. B. F. Kennedy, P. Wijesinghe, and D. D. Sampson, "The emergence of optical elastography in biomedicine," Nat. Photon. **11**, 215–221 (2017).
13. K. M. Kennedy, R. A. McLaughlin, B. F. Kennedy, A. Tien, B. Latham, C. M. Saunders, and D. D. Sampson, "Needle optical coherence elastography for measurement of microscale mechanical contrast deep within human breast tissues," J. Biomed. Opt. **18**(12), 121510 (2013).
14. A. Curatolo, M. Villiger, D. Lorenser, P. Wijesinghe, A. Fritz, B. F. Kennedy, and D. D. Sampson, "Ultrahigh resolution optical coherence elastography," Opt. Lett. **41**(1), 21–24 (2016).
15. A. Curatolo, P. R. T. Munro, D. Lorenser, P. Sreekumar, C. C. Singe, B. F. Kennedy, and D. D. Sampson, "Quantifying the influence of Bessel beams on image quality in optical coherence tomography," Sci. Rep. **6**, 23483 (2016).
16. P. Wijesinghe, N. J. Johansen, A. Curatolo, D. D. Sampson, R. Ganss, and B. F. Kennedy, "Ultrahigh-resolution optical coherence elastography images cellular-scale stiffness of mouse aorta," Biophys. J. (in press), (2017).
17. T. Xie, S. Guo, Z. Chen, D. Mukai, and M. Brenner, "GRIN lens rod based probe for endoscopic spectral domain optical coherence tomography with fast dynamic focus tracking," Opt. Express **14**(8), 3238–3246 (2006).
18. R. S. Pillai, D. Lorenser, D. D. Sampson, "Deep-tissue access with confocal fluorescence microendoscopy through hypodermic needles," Opt. Express **19**(8), 7213–7221 (2011).
19. D. M. Huland, C. M. Brown, S. S. Howard, D. G. Ouzounov, I. Pavlova, K. Wang, D. R. Rivera, W. W. Webb, and C. Xu, "*In vivo* imaging of unstained tissues using long gradient index lens multiphoton endoscopic systems," Biomed. Opt. Express **3**(5), 1077–1085 (2012).
20. Jun Ki Kim, Woei Ming Lee, Pilhan Kim, Myunghwan Choi, Keehoon Jung, Seonghoon Kim, and Seok Hyun Yun, "Fabrication and operation of GRIN probes for *in vivo* fluorescence cellular imaging of internal organs in small animals," Nat. Protoc. **7**(8), 1456–1469 (2012).
21. B. A. Flusberg, E. D. Cocker, W. Piyawattanametha, J. C. Jung, E. L. M. Cheung, and M. J. Schnitzer, "Fiber-optic fluorescence imaging," Nat. Methods **2**, 941–950 (2005).
22. B. F. Kennedy, R. A. McLaughlin, K. M. Kennedy, L. Chin, A. Curatolo, A. Tien, B. Latham, C. M. Saunders, and D. D. Sampson, "Optical coherence micro-elastography: mechanical-contrast imaging of tissue microstructure," Biomed. Opt. Express **5**(7), 2113–2124 (2014).
23. B. F. Kennedy, S. H. Koh, R. A. McLaughlin, K. M. Kennedy, P. R. T. Munro, and D. D. Sampson, "Strain estimation in phase-sensitive optical coherence elastography," Biomed. Opt. Express **3**(8), 1865–1879 (2012).
24. K. M. Kennedy, L. Chin, R. A. McLaughlin, B. Latham, C. M. Saunders, D. D. Sampson, and B. F. Kennedy, "Quantitative micro-elastography: imaging of tissue elasticity using compression optical coherence elastography," Sci. Rep. **5**, 15538 (2015).
25. R. Ganss and D. Hanahan, "Tumor microenvironment can restrict the effectiveness of activated antitumor lymphocytes," Cancer Res. **58**(20), 4673–4681 (1998).
26. W. M. Lee and S. H. Yun, "Adaptive aberration correction of GRIN lenses for confocal endomicroscopy," Opt. Lett. **36**(23), 4608–4610 (2011).
27. B. F. Kennedy, R. A. McLaughlin, K. M. Kennedy, L. Chin, P. Wijesinghe, A. Curatolo, A. Tien, M. Ronald, B. Latham, C. M. Saunders, and D. D. Sampson, "Investigation of optical coherence microelastography as a method to visualize cancers in human breast tissue," Cancer Res. **75**(16), 3236–3245 (2015).
28. C. Wang and N. Ji, "Pupil-segmentatin-based adaptive optical correction of a high-numerical-aperture gradient refractive index lens for two-photon fluorescence endoscopy," Opt. Lett. **37**(11), 2001–2003 (2012).
29. M. Wojtkowski, V. J. Srinivasan, T. H. Ko, J. G. Fujimoto, A. Kowalczyk, and J. S. Duker, "Ultrahigh-resolution,

Biomedical Optics EXPRESS

high-speed, Fourier domain optical coherence tomography and methods for dispersion compensation," Opt. Express **12**(11), 2404–2422 (2004).
30. L. Dong, P. Wijesinghe, J. T. Dantuono, D. D. Sampson, P. R. T. Munro, B. F. Kennedy, and A. A. Oberai, "Quantitative compression optical coherence elastography as an inverse elasticity problem," IEEE J. Sel. Top. Quantum Electron. **22**(3), 6802211 (2016).

1. Introduction

From the macroscopic to the microscopic scale, mechanical properties of tissue play an important role in the onset and progression of disease. In many cases, disease is accompanied by a modification of such properties. For example, breast cancer often presents as a stiff lesion and atherosclerotic plaques are typically stiffer than surrounding arterial tissue [1]. To improve understanding of disease processes and to provide advanced diagnostic capabilities, over the last 30 years, a collection of imaging techniques, known as elastography, have been developed to image the mechanical properties of tissue [2]. These techniques were initially based on ultrasound (US) [3] and magnetic resonance imaging (MRI) [4], and are mainly applied to clinical diagnosis on a macroscopic scale. On the other hand, on a microscopic scale, techniques such as atomic force microscopy (AFM) [5] and traction force microscopy (TFM) [6] have been developed to measure cell mechanical properties and have shown that mechanical properties play a role in both the genesis and progression of many diseases [1]. Over the last 10 years, on the scale intermediate between the macroscopic and microscopic, optical elastography has been developed to open a new window into "meso-scale" mechanical properties of tissue. A number of optical elastography techniques have been developed, based on, for example, optical coherence tomography (OCT) [7], Brillouin microscopy [8] and laser speckle microscopy [9]. Optical coherence elastography (OCE) [10–12], in particular, holds promise for *in vivo* imaging of tissue mechanics due to its combination of high resolution, rapid imaging speed and compatibility with compact imaging probes [13].

The majority of OCE techniques are limited in resolution to 10–100 μm [10]. Recently, an ultrahigh-resolution optical coherence elastography (UHROCE) technique (1.5 μm axial, 1.6 μm lateral optical resolution) has been developed by combining compression elastography with an optical coherence microscopy (OCM) system with Bessel beam illumination and Gaussian mode detection, providing ultrahigh-resolution whilst extending the depth-of-field (DOF) over systems using both Gaussian illumination and detection [14–16]. UHROCE opens new possibilities for imaging cellular-scale mechanics, complementing existing techniques such as AFM [5], and holds promise for cellular-scale mechanical imaging *in vivo* and in three dimensions: providing depth-resolved measurements to hundreds of micrometers below the tissue surface. Measurements beyond the vicinity of the tissue surface, however, require the development of an imaging probe that can provide access to sub-surface tissue structure. This can be achieved through gradient-index (GRIN) rod lenses. GRIN lenses are ideal components in the construction of small diameter optical probes, due to their propensity for miniaturization, enabled by a parabolic refractive index distribution along the radius in the GRIN lens material. Recently, GRIN lens endoscopes have been incorporated into different imaging systems to enable *in vivo* measurements, including OCT [17], confocal microscopy [18] and multiphoton microscopy [19]. A group of GRIN lenses, working as a single optical component, has also been used in imaging systems, for example, in *in vivo* cellular-scale fluorescence imaging [20].

In this paper, we present the first demonstration of endoscopic UHROCE with a triplet GRIN lens micro-endoscope. To the best of our knowledge, it is the first demonstration that Bessel beams can be effectively relayed through a GRIN lens assembly to enable extended-focus imaging. Similar probes have previously been used for an endoscopic implementation of confocal [21] and multiphoton microscopy [20]. The rigid micro-endoscope enables *in situ* or *in vivo* UHROCE measurements from below the tissue surface. An important feature of our probe is its capacity to

Biomedical Optics EXPRESS

relay the Bessel beam illumination to the tissue, whilst preserving the extended focus (from 94 μm DOF before the micro-endoscope to 80 μm after). In this paper, we present a characterization of the lateral and axial resolution of the Bessel beam before and after the micro-endoscope using a point spread function (PSF) phantom. We demonstrate UHROCE through the micro-endoscope on a silicone phantom with a rigid inclusion and on tissue excised from a murine model of pancreatic cancer. To move toward *in vivo* measurement, we also demonstrate the feasibility of this system directly on a murine sample *in situ* by measuring strain micro-elastograms of muscle ~200 μm below the tissue surface.

2. Methods

Figure 1(a) shows the optical layout of the UHROCE system. The super-continuum light source (SuperK Extreme EXR-1, NKT Photonics, Denmark) is spectrally shaped to a central wavelength of 785 nm and 3 dB bandwidth of 200 nm. Light from the source is split by a broadband fiber coupler into a reference arm maintaining a Gaussian profile, and a sample arm including a spatial light modulator (SLM) (Pluto NIR II-HR, Holoeye Photonics AG, Germany), configured to provide a Bessel beam (Fresnel number N=10.5) [14, 15]. The Bessel beam illumination after the objective lens (OL) has an effective numerical aperture (NA) of 0.27. The beam focused by the OL propagates through a GRIN lens system, which acts as the micro-endoscope. The GRIN lens system comprises three GRIN elements: a coupling lens (GoFoton SLW-100, 0.25 pitch), a relay lens (GoFoton, SRL-100, 1.0 pitch) and an imaging lens (GoFoton SLW-100, polished to 0.23 pitch). The assembly is similar to that previously used in multiphoton microscopy [20]. The coupling lens has an NA of 0.42 and is placed at the focal point of the OL to couple the Bessel beam into the GRIN lens system. The low-NA relay lens (NA=0.1) is used to transfer the beam from the coupling lens to the imaging lens, which also has an NA of 0.42. Each element has a diameter of 1 mm and the assembly is glued together to make a compound lens with a total length of 53 mm. For protection, the micro-endoscope is encased within a cylindrical stainless-steel shell with an outer diameter of 1.25 mm. The working distance of the micro-endoscope is 150 μm in air. In Fig. 1, the propagation of the beam through the micro-endoscope is shown schematically for both *ex vivo* (Fig. 1(b)) and *in situ* (Fig. 1(c)) scenarios. The Bessel beam profiles before and after the micro-endoscope are measured with a beam profiler (SP620U, Ophir-Spiricon, USA) and the lateral and axial optical resolutions are characterized using a PSF phantom, comprising iron oxide (Fe_2O_3) particles (refractive index, n≈3) with a diameter of 300-800 nm, embedded in polyurethane resin (n=1.49) (National Physical Laboratory, UK). The results of this characterization are described in Section 3.

Two mechanical loading configurations were used in this study. For the phantom and *ex vivo* results presented in Section 3, mechanical loading was provided by an annular piezoelectric actuator (PA) driving the side of the sample opposite to the imaging direction, as shown in Fig. 1(b). A glass plate was fixed to the actuator surface and acts both as a sample stage and a compression plate. The sample, placed between the glass plate and the micro-endoscope, was preloaded to ensure good contact. The PA provided step-wise micron-scale compression of the sample synchronized with OCM B-scans. The sample's local axial displacement, in response to compression, was measured using phase-sensitive detection described in detail previously [22,23]. The local axial strain was calculated as the change in the local axial displacement with depth, estimated over an axial range of 50 μm at each pixel in the dataset, using a weighted least squares method described previously [23]. This resulted in an axial resolution of 50 μm in the elastograms imaged by the system. The local axial strain was mapped into a three-dimensional (3-D) strain micro-elastogram. To measure the elasticity of the phantom and tissue, a quantitative compression OCE technique was used, where a thin compliant layer (90 μm thick) with well-known mechanical properties was placed between the endoscope and the tissue to map stress at the tissue surface [24]. The stress, which is assumed to be uniform with depth, was used alongside the local axial strain,

Biomedical Optics EXPRESS

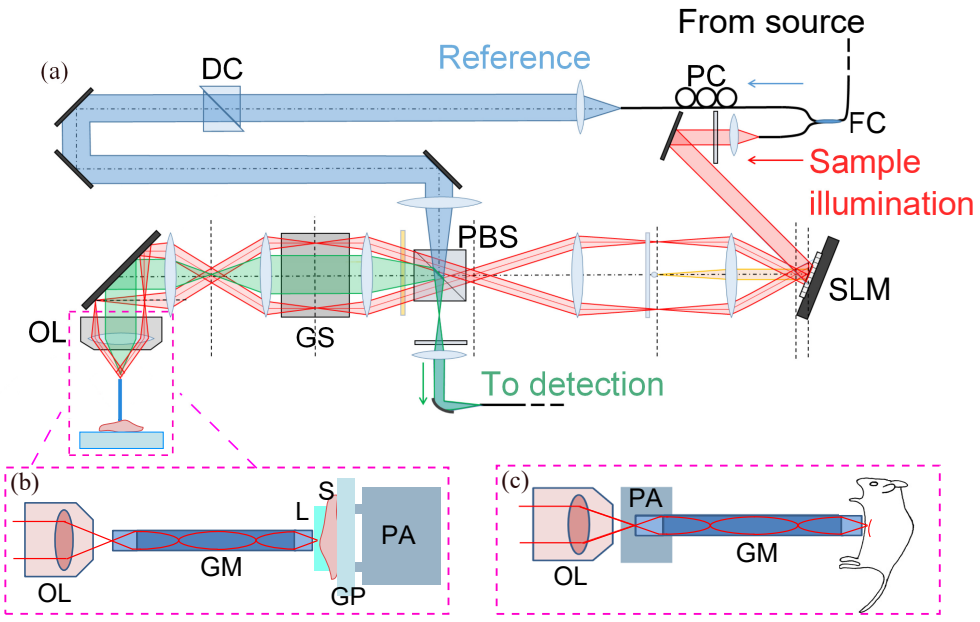

Fig. 1. (a) Schematic of the UHROCE system. DC, dispersion compensation; FC, fiber coupler; GS, galvanometer scanning mirrors; OL, objective lens; SLM, spatial light modulator (angle exaggerated); PBS, polarizing beam splitter; PC, polarization controller; $\lambda/4$, quarter-wave plate. (b) Enlarged drawing of the GRIN lens micro-endoscope setup used for phantom and *ex vivo* tissue measurements. GM, GRIN lens micro-endoscope; GP, glass plate; L, compliant layer; PA, piezoelectric actuator; S, sample. (c) Drawing of the micro-endoscope setup used for the *in situ* measurement. Figure components are not to scale.

measured in three dimensions in the sample, to estimate the Young's modulus (or, more accurately, the tangent modulus, since the soft tissue sample are generally nonlinear elastic materials) via Hooke's Law. In this paper, we present *en face* images, as ultrahigh-resolution elastograms in our method are preserved in the *xy*-planes.

The first configuration, however, is not suitable for *in situ* measurements as it would require significant amount of force to move the animal and induce measurable local deformations. Therefore, instead of driving the sample with that PA, we integrated micro-endoscope with PA (Fig. 1(c)) and used the endoscope as a quasi-static compression mechanism. Besides this modification to the actuation mechanism, the experimental setup and signal processing were identical to those already described. The extension of the micro-endoscope beyond the PA is 30 mm. OCM images and strain micro-elastograms were obtained from this setup.

To acquire 3-D datasets, two galvanometer scanning mirrors (GS) were used to scan the beam over the sample in orthogonal (x and y) directions. The line period of each OCM A-scan is 100 μs. There are 1,000 A-scans in each B-scan over a scanning range of 300 μm, resulting in a lateral pixel size of 0.3 μm. There are 10,000 B-scans in each C-scan over the scanning range of 300 μm, with two B-scans acquired at each location. This results in a lateral pixel size of 0.06 μm. The PA was driven by a square-wave, synchronized with each B-scan pair, such that a B-scan of the unloaded and loaded sample were captured sequentially at the same location. The total acquisition time is ~16 minutes to scan a region of 300×300 μm^2. The field-of-view of the micro-endoscope is 200 μm in diameter, limited by the high NA of the Bessel beam and the diameter of the GRIN elements. In post-processing, 5 pairs of B-scans are averaged at the same pixel location to increase both the strain and elasticity sensitivity. To increase contrast, the strain

Biomedical Optics EXPRESS

and quantitative micro-elastograms are averaged over a range of 1.5 μm laterally to match the optical resolution.

To demonstrate the capabilities of our system, we imaged a soft silicone phantom (tangent modulus = 80 ± 20 kPa) containing a stiff inclusion (tangent modulus = 250±20 kPa), a freshly excised murine pancreatic tumor, and *in situ* murine muscle below the tissue surface. The silicone phantom comprises a bulk material (Wacker P7676, part A:B mixing ratio 1:1) with a diameter of 10 mm and a thickness of 1 mm. A rigid silicone inclusion (Wacker RT601, part A:B mixing ratio 5:1), ~200×100×100 μm^3, was embedded in the bulk material, to provide high mechanical contrast. To introduce optical scattering contrast, titanium dioxide particles, with a concentration of 3 mg/ml, were added to the inclusion. The particles were added when the inclusion was fabricated and were stirred by a cylindrical magnetic bar. The particles could be unevenly diffused and distributed in small scales. We used a scalpel blade to cut the inclusion under a microscope. Due to the small size required for imaging within the field-of-view of the micro-endoscope, it was difficult to cut the inclusion into a regular cuboid with sharp edges and smooth facets. In addition, the side facets of the inclusion were not parallel to the axial axis of the imaging system, causing a gradient mechanical measurement. The compliant layer used for elasticity measurements was fabricated from the same compound as the bulk material of the inclusion phantom, with a thickness of 90 μm. Both the compliant layer and the bulk material have no titanium dioxide particles added, as the layer is required to be as transparent as possible to allow maximum incident light on the sample and the intrinsic scattering in the bulk is sufficient to generate a speckle pattern. The murine tumor was freshly excised from a transgenic mouse model which develops pancreatic cancer of neuroendocrine origin [25]. The tumor sample was placed in phosphate buffered saline (PBS) for approximately one hour after excision and was then positioned on the sample stage. The tumor sample was ~5×5×2 mm^3 in volume. Whole tumor was embedded in optimal cutting temperature (O.C.T.) compound and stored at −80 °C for further histological analysis. A serial 8-μm tumor tissue cross-section was stained with hematoxylin and eosin (H&E) and imaged microscopically (Aperio Scanscope XT, 20x magnification). The murine body was measured *in situ* within one hour post-mortem. The skin on the chest area was removed. The micro-endoscope was directly loaded onto the exposed tissue and the muscle below the tissue surface was imaged. The use of the pancreatic tumor from experimental mice was approved by the Animal Ethics Committees of The University of Western Australia. The *in situ* animal tissue experiment was approved under institutional tissue-sharing protocols.

3. Results

To characterize the system, we first compare the beam profiles before and after the micro-endoscope with a beam profiler. Figures 2(a) and 2(b) show lateral beam profiles before and after the micro-endoscope, respectively. It is clear in Fig. 2(b) that the shape of the Bessel beam after the micro-endoscope is well-maintained. In the first ring around the central bright spot in each of the lateral beam profiles in Figs. 2(a) and 2(b), there are unwanted bright lobes marked using white arrows in the embedded inserts. The bright lobes are likely caused by diffraction of the pixelated axicon phase mask in the SLM. The orientation of the lobes in Fig. 2(b) is turned ~180° from that in Fig. 2(a), as the lateral beam profile is inverted by 180° after propagation through the triplet GRIN lens system. The absolute light intensity in Figs. 2(a) and 2(b) are not equal. In Fig. 2(a), the input light intensity was reduced to avoid saturation on the central spot of the beam profile. In Fig. 2(b), the input light intensity was increased to compensate for reduction in intensity after propagation through the micro-endoscope. Figures 2(c) and 2(e) are axial beam profiles of the Bessel beam, respectively, before and after the micro-endoscope across the plane containing the central lobe with maximum light intensity, with the color bars representing normalized light intensity. Figure 2(e) shows that, the Bessel beam shape is well-maintained after the micro-endoscope, with 15% reduction in the DOF (full-width-at-half-maximum (FWHM))

Biomedical Optics EXPRESS

from 94 μm to 80 μm. Figures 2(d) and 2(f) are plots of the maximum light intensity along the axial direction for the two axial beam profiles in Figs. 2(c) and 2(e). The reduction in the DOF is most likely due to the imperfect alignment and optical aberrations of the GRIN lenses. This issue is discussed in more detail in Section 4.

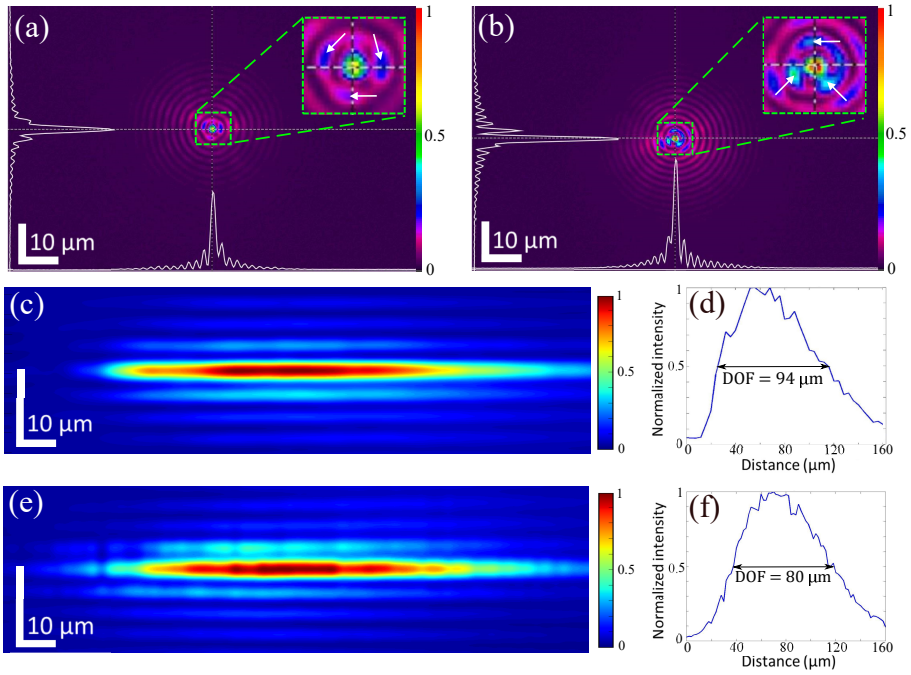

Fig. 2. Bessel beam profiles before and after the micro-endoscope. *En face* Bessel beam profile at focus (a) before and (b) after the micro-endoscope. Axial Bessel beam profile (c) before and (e) after the micro-endoscope. Maximum light intensity projection along the axial direction at focus (d) before and (f) after the micro-endoscope. DOF, depth-of-field.

We characterized the imaging performance of the micro-endoscope by measuring a PSF phantom before and after the micro-endoscope. As the particle size in the PSF phantom is much smaller than the spatial resolution of the imaging system, images of the particles represent the PSF of the imaging system. The results are shown in Fig. 3. Figures 3(a) and 3(b) are OCM *en face* images of a particle at focus before and after the micro-endoscope. Figures 3(c) and 3(d) are OCM B-scans of a particle at focus before and after the micro-endoscope. Figures 3(e) and 3(f) are plots of the OCM signal-to-noise ratios (SNRs) along the horizontal and vertical dashed lines in Fig. 3(a), respectively. The x and y lateral optical resolutions of the system before using the micro-endoscope are defined as the 6 dB widths of Figs. 3(e) and 3(f), which are 1.6 μm and 1.4 μm, respectively. The lateral optical resolution, calculated by averaging the x and y resolutions, is 1.5 μm. The axial optical resolution before using the micro-endoscope is 1.7 μm, which is defined as the 6 dB width of Fig. 3(g): the SNR plot along the vertical dashed line in Fig. 3(c). In comparison, the x and y lateral optical resolution after the micro-endoscope are 1.4 μm and 1.8 μm, measured from 3(h) and 3(i). The lateral optical resolution is 1.6 μm after averaging the x and y lateral resolutions. The axial optical resolution after the micro-endoscope is characterized as 2.2 μm from Fig. 3(j): the SNR plot along the vertical dashed line in Fig. 3(d). Note that both the lateral and axial optical resolutions after the micro-endoscope degrade from that before the micro-endoscope. We believe that the lateral optical resolution degradation is caused by the optical aberrations introduced by non-aplanatic properties of the GRIN lenses [26],

Biomedical Optics EXPRESS

and the axial optical resolution degradation is mainly due to optical dispersion introduced by the micro-endoscope. Both aspects will be discussed in more detail in Section 4.

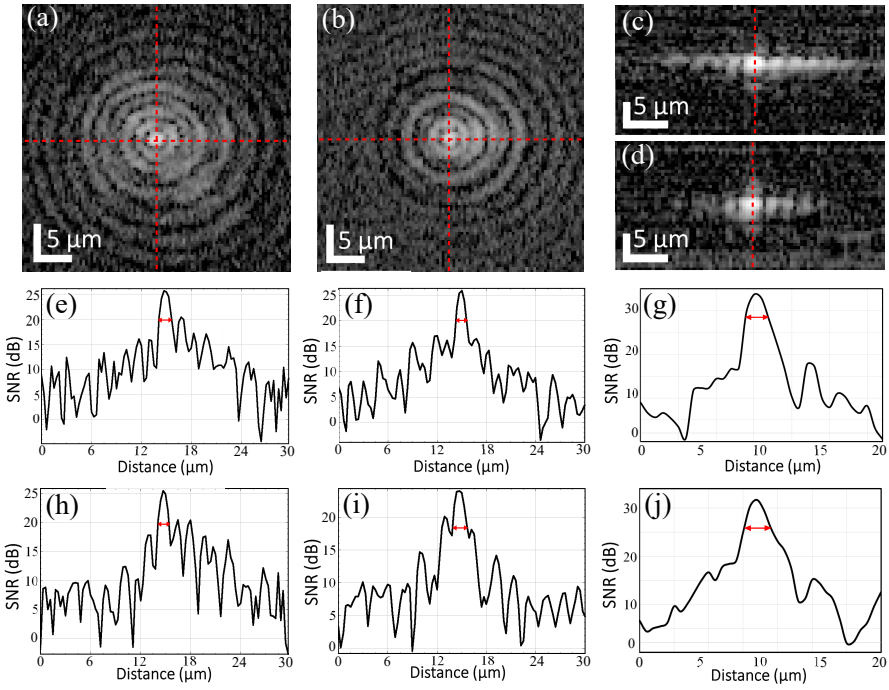

Fig. 3. PSF characterization. *En face* OCT image of a particle at focus in a PSF phantom imaged (a) before and (b) after the micro-endoscope; OCT B-scan of a particle at focus in the PSF phantom (c) before and (d) after the micro-endoscope. (e) and (f) SNR profiles along the horizontal and vertical red dashed lines in (a). (h) and (i) SNR profiles along the horizontal and vertical red dashed lines in (b). (g) and (j) SNR profiles along the vertical red dashed line in (c) and (d), respectively. Double-headed arrows are labelled for characterized resolutions in (e)-(j).

The results from the silicone phantom with a rigid inclusion are shown in Fig. 4. Figure 4(a) presents the *en face* OCM image of the phantom. The near-rectangular inclusion is 170 μm long and 70 μm wide. Due to the titanium dioxide particles added to the inclusion, it displays higher optical scattering than the surrounding bulk material, resulting in a high OCM SNR in the corresponding region. The edges of the inclusion have a gradient, as described previously, caused by manually cutting with the scalpel blade. The *en face* OCM image was taken at a depth of 100 μm under the phantom surface. Figure 4(b) is the corresponding *en face* quantitative micro-elastogram, demonstrating the higher elasticity of the inclusion versus the bulk material. In Fig. 4(b), the average elasticity of the inclusion is 290±90 kPa and the average elasticity of the bulk material is 90±40 kPa. These results are within 15% error of the characterization performed using in-house built uniaxial compression tester for the two materials (250±20 kPa for the inclusion and 80±20 for the bulk material). The discrepancies are most likely due to an error in layer thickness estimation. In Fig. 4(b), an artifact due to phase unwrapping errors has been removed by fusing two *en face* micro-elastograms at the same depth processed with the same data, but different phase unwrapping parameters [14].

To demonstrate the feasibility of UHROCE with a micro-endoscope on biological tissues, we measured freshly excised malignant murine pancreatic tumor, as shown in Fig. 5. A region at the boundary between a red-colored area and a white/grey-colored area, as visible in the specimen

Biomedical Optics EXPRESS

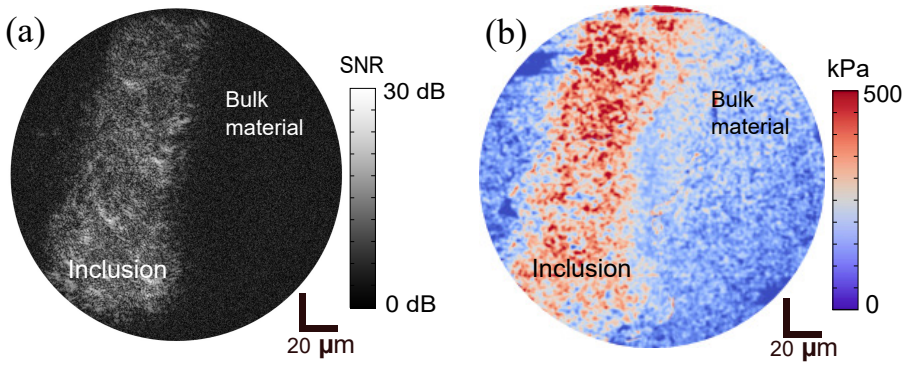

Fig. 4. *En face* (a) OCM image and (b) quantitative micro-elastogram of the phantom at a depth of 100 μm.

photograph (Fig. 5(c)), was selected for scanning. After scanning, the area indented by the micro-endoscope was visible to the naked eye, and highlighted in Fig. 5(c) (green dashed circle). Figure 5(a) presents an *en face* OCM image at an imaging depth of 100 μm from the tissue surface. Figure 5(b) is an *en face* quantitative micro-elastogram at the same spatial location. The black arrows in Fig. 5(b) indicate a stiff area in the tumor, with an elasticity of 80±20 kPa, while the surrounding area displays a lower elasticity of 20±10 kPa. The quantitative micro-elastogram shows a heterogeneous elasticity distribution over the scanned area of the tumor. The region of high elasticity corresponds to a region of high OCM signal in Fig. 5(a). Figure 5(c), the photograph of the sample, shows visually the heterogeneity in this hemorrhagic tumor mass. The heterogeneity of the tumor is also indicated in Fig. 5(d), which is a representative H&E staining histology of the tumor at around 100 μm below the surface of the scan area. In the enlarged subfigure of the histology, which corresponds approximately to the scan area, cancer cells and extracellular matrices can be identified.

Next, UHROCE through a micro-endoscope was demonstrated in a murine body *in situ*, using the modified experimental setup displayed in Fig. 1(c). In this setup, the PA was placed to drive the micro-endoscope and the compliant layer was not in use. The results are shown in Fig. 6. Figure 6(a) presents an *en face* OCM image of murine muscle 230 μm below the tissue surface. Figure 6(b) presents the corresponding *en face* strain micro-elastogram of the same spatial location as in Fig. 6(a), at the same depth as the OCM image. A region of high strain in Fig. 6(b) is highlighted by a blue arrow. This high strain was caused by a rib underlying the muscle, as the muscle was compressed more in this case. The lateral expansion of the compressed tissue could lead to a vertical bulging in the surrounding tissue, resulting in the negative strain. This has been observed and discussed in more detail in our previous work in optical elastography of breast tissue [27]. The rib underlying the tissue can be indicated by the OCM images through the depth, where dark area with low optical signals appears from a depth of 350 μm. The micro-endoscope mounted on the PA and the experimental murine body in the *in situ* setup is shown in the photograph in Fig. 6(c).

4. Discussion

In this paper, we have demonstrated UHROCE through a micro-endoscope. Endoscopic UHROCE has potential for cellular-scale imaging of the mechanical properties of living tissue. In this first demonstration, we characterized the imaging system and performed imaging of both the phantom and tissue by placing the micro-endoscope at the sample surface. In the *in situ* setup, although the images shown in this paper are ~200 μm below the tissue surface, the micro-endoscope could

Biomedical Optics EXPRESS

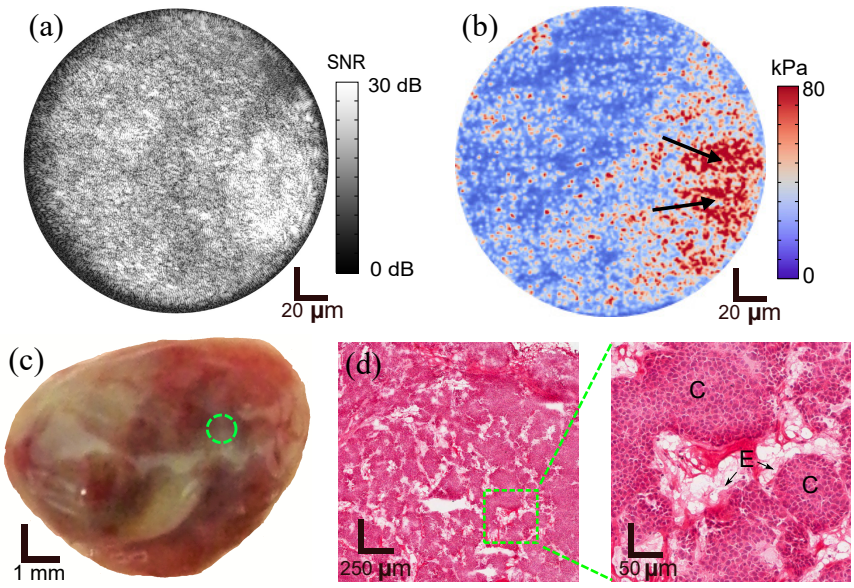

Fig. 5. *En face* (a) OCM image and (b) quantitative micro-elastogram of the freshly excised murine pancreatic tumor at a depth of 100 μm. The black arrows indicate a stiff area in the tumor. (c) Photograph of the tumor. The green dashed circle indicates the indented area, which corresponds to the scanning location. The photograph is cropped around the tumor margin. (d) Representative H&E histology at 100 μm depth with an enlarged view of the approximate scan area. C, cancer cells; E, extracellular matrices.

penetrate as deeply as ~30 mm into the body. Beyond the proof-of-concept demonstration here, future work will aim to apply our technique to intravital longitudinal imaging of murine models.

Notwithstanding the power of this initial demonstration, there are aspects that can be improved. The fine alignment of the micro-endoscope and UHROCE objective lens was challenging and resulted in a degraded DOF after the micro-endoscope. There are six degrees of freedom in aligning the micro-endoscope: x, y, z translation, pitch, yaw, and roll. Although we were able to control all degrees of freedom by incorporating translation and tilt stages, it was difficult to find the optimum alignment by trial and error. In future work, a more robust method of alignment will be adopted, for example, by utilizing motorized translation and tilt stages to better register the micro-endoscope position.

The lateral and axial optical resolution slightly degrade after the micro-endoscope, as shown in Fig. 3. The lateral optical resolution degradation (from 1.5 μm to 1.6 μm) is mainly caused by the optical aberrations introduced by the parabolic refractive index distribution of the GRIN lenses. The optical aberrations also contribute to the DOF degradation of the Bessel beam. To overcome this degradation, adaptive-optic numerical methods [26, 28] could be used for wave-front and chromatic corrections. On the other hand, the axial optical resolution degradation (from 1.7 μm to 2.2 μm) is most likely caused by the unbalanced chromatic dispersion after adding the micro-endoscope to the system. Although an assembly of prism pairs was used in the reference arm to compensate the dispersion caused by the micro-endoscope, and satisfactory results were achieved, it was difficult to perfectly compensate in hardware for all residual dispersion. In future work, a numerical method [29] will be adopted in post-processing to compensate for the residual dispersion. In addition, the lateral and axial optical resolutions were characterized on one location within the field-of-view. Due to the alignment and optical aberrations of the GRIN lens assembly, the optical resolutions might slightly vary across the whole field-of-view.

Biomedical Optics EXPRESS

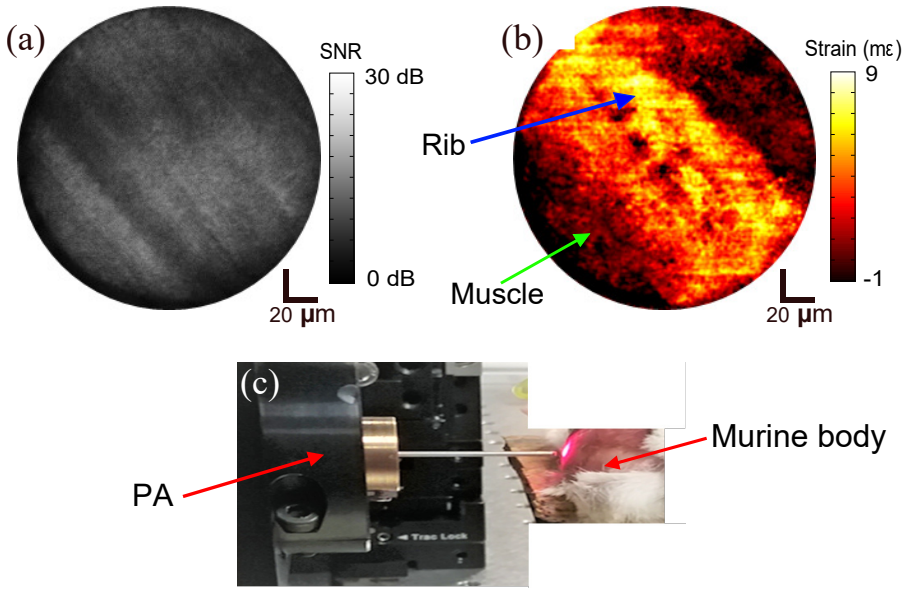

Fig. 6. *En face* (a) OCM image and (b) strain micro-elastogram at an imaging depth of 230 μm from the surface of the murine muscle. (c) Photograph of the *in situ* setup. The red light appears illuminating the sample is the scattering light in the visible wings of the spectrum. PA, piezoelectric actuator.

In the *ex vivo* tissue scanning, the histology was used to representatively demonstrate the heterogenous tumor structure. It was very challenging to achieve an accurate match between the micro-elastogram and histology, mainly due to the small scan area and uneven surface of the sample, coupled with the relatively shallow DOF of our imaging technique. Because our images are presented in the *en face* plane, histology is also required in this plane to allow optimum match. However, to cut through the tissue in the *en face* image plane was very difficult due to the surface unevenness. In the future, tissue regions with flat surfaces can be scanned and some small markers, for example, fluorescence particles, can be used to accurately match the scan area with histology, allowing optimal histological validation of the contrast in our image.

In the setup for *in situ* imaging, the compliant layer required to estimate stress for elasticity imaging was not used, due to the difficulty in placing the layer deep into the murine body. As a result, only the strain micro-elastograms were acquired with this setup. In future *in vivo* experiments, elasticity measurements are desired for which the compliant layer is required. To solve the stability issue, first the compliant layer will be cured directly to the micro-endoscope surface. Then a detailed characterization will be undertaken to analyze the effect of micro-endoscope motion on the image quality. Some modifications to the setup may be required to avoid motion of the micro-endoscope. For example, the actuator can be designed to drive the near-end of the sample. In addition, to use our technique *in vivo*, the image quality is expected to be susceptible to the motion of the sample, possibly requiring a higher scanning rate. Further extensions of this work may include fast scanning and acquisition methods.

In the *in situ* results, the high strain area represents the highly compressed tissue due to the underlying stiff rib. In this case, the generated strain micro-elastogram does not represent accurately the elasticity of the tissue imaged. With the help of the compliant layer as the stress sensor, the quantitative micro-elastogram could still be mapped for the tissue below the sample surface. Previous work of compression elastography assumes the stress is uniform along the

Biomedical Optics EXPRESS

axial axis so the stress map at the layer-sample interface represents the stress map of the whole sample volume. In such a case, the elastogram would be calculated from the stress map and local strain value at each location. Whilst this is true for homogeneous tissues, errors are introduced in complex tissues leading to some inaccuracy. However, numerical inversion methods can be used without the assumption of uniform stress, recovering the elasticity using only the measurements of axial displacement [30].

5. Conclusion

We have presented a novel UHROCE system comprising a micro-endoscope to enable cellular-scale elastography below the tissue surface. With the micro-endoscope incorporated, we have achieved comparable axial optical resolution (29% degradation from 1.7 μm to 2.2 μm), lateral optical resolution (7% degradation from 1.5 μm to 1.6 μm) and DOF (15% degradation from 94 μm to 80 μm) performance. We have measured the elasticity of an inclusion phantom, giving values within 15% of the expected values on both the bulk material and the inclusion. In addition, we have shown a quantitative micro-elastogram of a murine pancreatic tumor with a heterogenous elasticity distribution. With further modifications of the setup taking it closer to a setup capable of *in vivo* imaging, we have demonstrated strain contrast in murine muscle tissue *in situ*. We have shown that this technique has potential for *in vivo* cellular-scale imaging of mechanical properties.

Funding

This research was supported by grants and fellowships from the Australian Research Council, the National Health and Medical Research Council (Australia), the National Breast Cancer Foundation (Australia), the Department of Health, Western Australia, and the Cancer Council, Western Australia.

Acknowledgments

The authors acknowledge Martin Villiger and Dirk Lorenser for contributions to the design and construction of the UHROCE system.

Disclosures

BFK: OncoRes Medical (F,I), AC and DDS: OncoRes Medical (I). The other authors declare that there are no conflicts of interest related to this article.